

Article

Spatiotemporal Variation of Turbidity Based on Landsat 8 OLI in Cam Ranh Bay and Thuy Trieu Lagoon, Vietnam

Nguyen Hao Quang ^{1,*}, Jun Sasaki ² , Hiroto Higa ³ and Nguyen Huu Huan ⁴ 

¹ Institute of Marine Science and Fishing Technology, Nha Trang University, 02 Nguyen Dinh Chieu Street, Nha Trang 650000, Vietnam

² Sasaki Laboratory, Department of Socio-Cultural Environmental Studies, Graduate School of Frontier Sciences, the University of Tokyo, 5-1-5 Kashiwanoha Kashiwa, Chiba 277-8563, Japan; jsasaki@k.u-tokyo.ac.jp

³ Yokohama National University, 79-5 Tokiwadai, Hodogaya-ku, Yokohama 240-8501, Japan; higa-h@ynu.ac.jp

⁴ Institute of Oceanography, Vietnam Academy of Science and Technology (VAST), 01 Cau Da, Nha Trang 650000, Vietnam; nghhuan@gmail.com

* Correspondence: ri.nguyenri@gmail.com; Tel.: +84-933-566-290

Received: 12 April 2017; Accepted: 15 June 2017; Published: 8 August 2017

Abstract: In recent years, seagrass beds in Cam Ranh Bay and Thuy Trieu Lagoon have declined from 800 to 550 hectares, resulting insignificantly reducing the number of fish catch. This phenomenon is due to the effect of the degradation of water environment. Turbidity is one of the most important water quality parameters directly related to underwater light penetration which affects the primary productivity. This study aims to investigate spatiotemporal variation of turbidity in the waters with major factors affecting its patterns using remote sensing data. An algorithm for turbidity retrieval was developed based on the correlation between in situ measurements and a red band of Landsat 8 OLI with $R^2 = 0.84$ ($p < 0.05$). Simulating WAVes Nearshore (SWAN) model was used to compute bed shear stress, a major factor affecting turbidity in shallow waters. In addition, the relationships between turbidity and rainfall, and bed shear stress induced by wind were analyzed. It was found that: (1) In the dry season, turbidity was low at the middle of the bay while it was high in shallow waters nearby coastlines. Resuspension of bed sediment was a major factor controlling turbidity during time with no rainfall. (2) In the rainy season or for a short time after rainfall in the dry season, turbidity was high due to a large amount of runoff entering into the study area.

Keywords: remote sensing reflectance; turbidity; seagrass beds; bed shear stress; fresh water runoff; oceanic water intrusion

1. Introduction

Turbidity is an important water quality parameter and a surrogate for water clarity [1,2]. Turbidity can harm fish and other aquatic organisms by reducing feed supplies, degrading spawning grounds, and affecting gill function [3]. An increase or decrease in water clarity can negatively impact on biological components of the system that may be adapted to specific light-penetrating conditions [4,5]. In estuarine waters with high turbidity, the concentration of dissolved oxygen can dramatically decrease as a result of its imbalance between autotrophic and heterotrophic processes, which may lead to decline in marine organisms [6].

Traditionally, turbidity is estimated visually using a Secchi disk or measured directly with nephelometry [2,4]. In recent years, the technique of ocean color remote sensing has become a useful tool to map turbidity and suspended particulate matter concentration at surface in turbid coastal waters [7]. The strength of using remote sensing for water quality analysis is its ability to

capture synoptic data of a whole study area to produce continuous surface data, often showing detailed spatial variability in water quality [8]. While a number of remote sensing studies have been devoted to retrieving total suspended solids (TSS), studies on retrieving turbidity have been limited [7]. Even though satellite remote sensing cannot detect near-bed concentration, it can be used to study spatiotemporal variation of surface turbidity, and satellite-derived turbidity maps are valuable tools to study the influence of turbidity in shallow waters influenced by resuspension of bottom sediment and river plume dynamics.

Cam Ranh Bay and Thuy Trieu Lagoon opening to Vietnam East Sea/South China Sea (Figure 1) were known as the second largest seagrass area in Vietnam with abundant biotic resources contributing to development of aquaculture and marine production. The area, however, has decreased from 800 to 550 ha due to degradation of water environment [9] and marine resources as well as the number of fish catch have significantly decreased [10]. The study site is surrounded by hillocks and rivers; therefore, the turbidity and total suspended solids significantly increase when heavy rains bring increased inputs of suspended substances. High concentration of turbidity negatively affects aquaculture (seaweed, lobster and grouper) farming in Cam Ranh Bay and Thuy Trieu Lagoon.

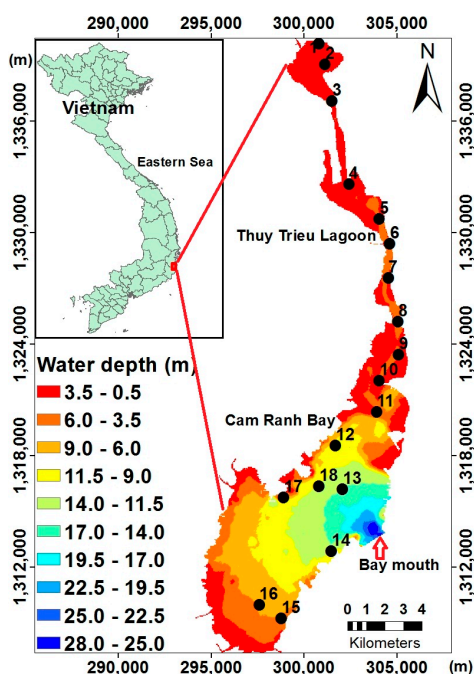


Figure 1. Location of the sampling stations (black points) and bathymetry of Cam Ranh Bay and Thuy Trieu Lagoon.

Estimation of turbidity distribution in complex environments like Cam Ranh Bay and Thuy Trieu Lagoon requires non-traditional approaches. Remote sensing techniques offer reliable advantages to observe and understand the variation in space and time and especially in large area with restricted access, e.g., military zones such as Cam Ranh Bay. Mapping turbidity as well as other water quality parameters has been routinely made using data from dedicated wide-swath ocean color instruments such as Orbview-2/SeaWiFS, Aqua/MODIS and ENVISAT/MERIS medium resolution images [11]. For small and narrow areas, however, such as the study site (the minimum width is just 250 m), these applications are inappropriate because their low spatial resolutions lead to numerous mixed pixels, resulting in an estimation with low precision. Compared with these medium resolution images, Landsat 8 Operational Land Imager (Landsat 8 OLI) has higher spatial resolution of 30 m. Landsat 8 has been widely used in coastal management and especially has been demonstrated to be a useful tool for monitoring of coastal sediment concentrations at high resolution and accuracy due to its higher signal-to-noise ratio (S/N)

compared to previous Landsat imagers [11]. Besides, Landsat 8 OLI has been innovated with 12 bits of radiance resolution compared to 8 bits for the older ones, Landsat 5 TM and Landsat 7 ETM+.

Numerous studies on ocean color remote sensing for water quality parameter retrieval have been done, most of which follow three main methods: (i) using semi-analytic models based on the correlation between the inherent optical properties (IOPs) and the water quality parameters [7,11–15]; (ii) using empirical models between IOPs and these parameters [1,16,17]; and (iii) using empirical models between remote sensing reflectance and the same parameters [18–21]. The third approach has been applied in this study, which is based on the correlation between remote sensing reflectance values extracted from Landsat 8 OLI and field measurements.

Using Cam Ranh Bay and Thuy Trieu Lagoon as a typical case study for turbid deep waters, the aim of this study is to determine the variation as well as major factors affecting the spatiotemporal patterns of turbidity. To achieve this, the following specific objectives must be satisfied: (1) estimating turbidity based on Landsat 8 OLI images and in situ measurements; and (2) analyzing its spatial and temporal variability along with their physical mechanisms.

2. Materials and Methods

2.1. Study Site

Cam Ranh Bay is an enclosed water located in the south of Khanh Hoa Province with approximately 19 km in length, 7 km in width and the average depth of 15 m while Thuy Trieu Lagoon is a narrow enclosed water connected with the north of the bay at Long Ho Bridge with approximately 16 km in length, 250 m in width and 0.5 to 6 m in depth. This water system consisting of the bay and the lagoon has the total area of approximately 119 km², the total length of 35 km and the average depth of 10 m parallel to the coast of central Vietnam (Figure 1) and connected to the East China Sea through the bay entrance with 1.2 km in width and 30 m in depth [22]. These waters are surrounded by sandy hill sand sheltered from winds. The study site represents aquaculture and fishing areas for sustaining more than 150,000 local people.

There are no major rivers entering into the bay and lagoon, but many streams or small rivers discharging into this area (Figure 2). Most of these streams/rivers have dams upstream to control and distribute the water in both dry and rainy season. Dams open during droughts (dry season) or when the water volume raises significantly (rainy season). Therefore, turbidity contributed from rivers to the study area is strongly influenced by the operation of the dams.



Figure 2. Dams and rivers surrounding study area (Google Earth).

During the dry season, these rivers have almost no water flowing into the Bay and Lagoon. In contrast, throughout the rainy season with high rainfall, the waters of the study area are affected by fresh water in the upper regions, reservoirs and rivers [10].

2.2. Field Survey

The availability of concurrent remote sensing and in situ data is considered a key element in this study. Field surveys were performed in Cam Ranh Bay and Thuy Trieu Lagoon on 16–19 September during the rainy season in 2015 and on 12–13 February during the dry season in 2016. The latter was performed concomitantly with a Landsat 8 OLI image obtained at 10:00 a.m. on 14 February 2016 to minimize the difference between in situ measurements and remotely sensing data. Because this is an enclosed water system with the resident times of more than 10 and 4 days [10] in dry and rainy seasons, respectively, one day lag is acceptable to develop turbidity algorithm.

Surface water samples and surface sediment samples were collected at 18 stations (Figure 1) using a water sampler, plastic cup, grab, and Petersen sediment samplers. Water quality parameters, including temperature, salinity, turbidity, and chlorophyll-a fluorescence, were measured using a multiple water quality sensor, AAQ 1186 (Alec Electronics), with the interval of 0.1 m in the vertical at the same 18 stations. Water and sediment samples were transferred to laboratory of Department of Marine Ecology, Institute of Oceanography, Nha Trang, Vietnam, immediately after the field measurements. Total suspended solids (TSS), chlorophyll-a, inorganic suspended solids (ISS) and organic suspended solids (OSS) were analyzed using the water samples while grain size distribution was determined using 18 sediment samples.

2.3. Analysis of Water and Sediment Samples

Total suspended solids (TSS) was determined using a vacuum filtration technique. TSS of a water sample was calculated by pouring a suitable measured volume of water (typically 1.5 to 2 liters but less if the particulate density was high) through a pre-weighed filter of a 0.45 μm pore size placed in a millipore filter holder and attach a controlled vacuum source which does not exceed approximately 1/3 atm, and then weighing the filter again after drying (in an oven at 103–105 $^{\circ}\text{C}$ for at least one hour in aluminum dish) to remove all the water [23]. TSS is the retained material on a standard glass fiber filter after filtration of a well-mixed sample divided by the total volume of sampled water in mg/L.

Organic suspended solids (OSS) was determined using a similar method as TSS by taking the difference between the original TSS and TSS after burning in an oven at 500 $^{\circ}\text{C}$. Inorganic suspended solids (ISS) was then calculated by subtracting OSS from TSS [23].

Chlorophyll-a (Chl-a) concentration was determined with an established in vitro laboratory analysis where a solvent was used to extract chlorophyll pigments from phytoplankton samples. The optical signals of the extracted pigments were then measured using a spectrophotometer [24,25]. In this study, absorbance of samples was measured at four wavelengths, 630, 647, 664 and 750 nm. Five or ten milliliters of acetone solution were used when concentration of algae was low or very high, respectively. Chl-a concentration was estimated by the formula of Jeffrey and Humphrey (1975):

$$\text{Chl-a (mg/m}^3\text{)} = (11.85E_{664} - 1.54E_{647} - 0.08E_{630}) \times V_{\text{acetone}} / V_{\text{water}} \quad (1)$$

where E_{664} , E_{647} and E_{630} are the absorptions of 664, 647 and 630 nm (after subtract absorption of E_{750}), respectively, V_{acetone} is the extracted volume of acetone (mL), and V_{water} is the volume of water sample [24].

Sediment grain size distribution was determined by sieve analysis (the mesh sizes in mm are 0.0001, 0.004, 0.016, 0.031, 0.083, 0.125, 0.25, 0.5, 1, 2, 4 and >4), commonly known as the gradation test. The top sieve has the largest screen openings and the screen opening sizes decrease with each sieve down to the bottom sieve which has the smallest opening size screen. During this process, the particles were compared with the apertures of every single sieve. The probability of a particle passing through

the sieve mesh was determined by the ratio of the particle size to the sieve openings, the orientation of the particle and the number of encounters between the particle and the mesh openings [26].

2.4. Meteorological and Oceanographic Data Collections

Observed meteorological data, including wind and precipitation, are very limited in this study area and no complete datasets are available for the purpose of our analysis. Instead, regarding wind data, a meteorological reanalysis dataset provided by National Center for Atmospheric Research Final (NCEP-FNL) Operational Model Global Tropospheric Analyses was collected covering the period from 2013 to 2016 with the geospatial and temporal resolutions of $1^\circ \times 1^\circ$ and 6 h, respectively. Rainfall data were obtained from NOAA CPC Morphing Technique (CMORPH) Global Precipitation Analyses that is available on the website of National Center for Atmospheric Research (NCAR). Its geospatial resolution is $0.25^\circ \times 0.25^\circ$ from 0.125° E to 359.875° E and 59.875° N to 59.875° S (1440×480 grids) and the temporal resolution is 3 h.

Tidal levels were calculated using NAOTIDE model developed by National Astronomical Observatory, Japan, which is designed to predict ocean tidal heights at any given time and location using an ocean tide model by assimilating TOPEX/POSEIDON altimeter data. Since the study area is small and short in length, it was assumed that tidal levels are uniform in the bay and lagoon and a representative point at the bay mouth (11.878142° latitude (lat.), 109.196341° longitude (long.)).

Besides, bathymetric data were provided by Institute of Oceanography with aspatial resolution of 200 m, measured in 2012.

2.5. Turbidity Retrieval Using Landsat 8 OLI

2.5.1. Image Acquisition

Remotely sensed data used for this study are Landsat 8 OLI at path 123 and row 52. Landsat 8 OLI images at L1T—Orthorectified products were downloaded freely from the website of United States Geological Survey (USGS) (<http://earthexplorer.usgs.gov/>).

Landsat 8 launched as the Landsat Data Continuity Mission on 11 February 2013, and is equipped with state-of-the-art imaging technology and other advancements to better collect data. Landsat 8 OLI has nine spectral bands ranging from 433 nm to 1390 nm at 30 m spatial resolution and one panchromatic channel at 15 m spatial resolution. This is a sun-synchronous orbiting satellite with an altitude of 705 km, an orbital inclination of 98.2° , and a circle time of 98.8 min around the earth. Landsat 8 OLI has been innovated with 12 bit of radiance resolution compared to 8 bit for the older ones, Landsat 5 TM and Landsat 7 ETM+. In addition, the OLI sensor employs push broom scanner technology that enables data acquisition with much better performance in terms of the signal-to-noise ratio (S/N) and higher radiometric resolution [15]. Specification of Landsat 8 OLI is summarized in Table 1.

Table 1. Specification of Landsat 8 OLI.

Landsat 8	
Band Description (30 m Native Resolution unless Otherwise Denoted)	Wavelength (μm)
Band 1—blue	0.43–0.45
Band 2—blue	0.45–0.51
Band 3—green	0.53–0.59
Band 4—red	0.64–0.67
Band 5—near infrared	0.85–0.88
Band 6—shortwave infrared	1.57–1.65
Band 7—shortwave infrared	2.11–2.29
Band 8—panchromatic (15 m)	0.50–0.68
Band 9—cirrus	1.36–1.38
Band 10—thermal infrared (100 m)	10.60–11.19
Band 11—thermal infrared (100 m)	11.50–12.51

Landsat 8 OLI images at L1T after system radiation correction and geometry correction [15] were collected with less cloud cover, no rain, high visibility and suitable conditions. Totally, 18 high quality images (Table 2) were used to estimate turbidity in Cam Ranh Bay and Thuy Trieu Lagoon. Each scene was downloaded as zipped folder containing TIFF images of the scene for each band and accompanying metadata file.

Table 2. Date acquisition and cloud cover (%) of Landsat 8 OLI images obtained.

No.	Cloud Cover (%)	Date Acquisition	No.	Cloud Cover (%)	Date Acquisition
1	5.00	14 February 2016	10	1.60	15 March 2015
2	5.50	9 October 2015	11	3.41	26 January 2015
3	2.50	23 September 2015	12	0.55	20 September 2014
4	0.49	7 September 2015	13	4.03	2 July 2014
5	4.52	22 August 2015	14	17.10	15 May 2014
6	15.63	6 August 2015	15	8.34	12 March 2014
7	8.23	21 July 2015	16	2.51	8 February 2014
8	6.03	3 June 2015	17	0.24	16 August 2013
9	3.66	16 April 2015	18	0.28	29 June 2013

2.5.2. Masking

Before atmospheric correction, only the water body should be retained and the rest needs to be masked. Masking of the Landsat imagery was performed using ArcGIS software Version 10.2.2. An area of interest was extracted as shapefiles using Google Earth and imported onto ArcGIS (.evf file) and overlaid on Landsat 8 OLI image. Using a masking tool embedded in ArcGIS, only the water area was retained. This process is required to obtain better contrast stretch of study area, to remove meaningless pixels and to eliminate the noises from other objects irrelevant to the main targets. Masking technique can also hide cloud cover that is the main source of noises and distortions of the satellite images.

2.5.3. Atmospheric Correction

There is a variety of atmospheric correction methods and associated models, such as DOS (Dark Object Subtraction), FLAASH (Fast Line-of-sight Atmospheric Analysis of Spectral Hypercubes), 6S (Second Simulation of the Satellite Signal in the Solar Spectrum), QUAC (Quick Atmospheric Correction), etc. Among them, FLAASH is one of the most widely used tools because of its higher accuracy and easier use compared to the others [14,20,27–30].

FLAASH model, which is a MODTRAN-based “atmospheric correction” software package, embedded in ENVI software is a strong tool for atmospheric correction [29]. FLAASH is a first-principles atmospheric correction tool that corrects wavelengths in the visible through near-infrared and shortwave infrared regions, up to 3 μm [31]. In this study, FLAASH method was applied to retrieve reflectance from the surface.

In the first step of atmospheric correction process, radiometric calibration, image data were converted from brightness values in digital number (D_{br}) into radiance at top of atmosphere, L_{TOA} . Gain and offset values from the image header files were used.

$$L_{TOA} = M_L D_{br} + A_L \quad (2)$$

where M_L is multiplicative factor (gain) and A_L is additive factor (offset) provided in the metadata file. Subsequently, radiance at the top of atmosphere was converted to the non-dimensional reflectance at the top of atmosphere, ρ_{TOA} , defined as the reflectance measured by a space-based sensor flying higher than the earth’s atmosphere. The reflectance at the top of atmosphere was computed by normalizing L_{TOA} to the band averaged solar irradiance:

$$\rho_{TOA} = \frac{\pi L_{TOA} d^2}{ESUN_{\lambda} \cos \theta_s} \quad (3)$$

where d is Earth–Sun distance in astronomical units; $ESUN_{\lambda}$, the direct solar radiation component, is mean solar exoatmospheric irradiances; and θ_s is solar zenith angle.

Converting reflectance at the top of the atmosphere (ρ_{TOA}) into surface reflectance is the next step in the atmospheric correction process. The key parameters used in the FLAASH module of ENVI were: *tropical* for atmospheric model, *tropospheric* for the aerosol model because the study area is far from urban or industrial locations belonging to tropical area, and 2-band (K-T) for the aerosol retrieval; initial visibility was chosen as 40 km, depending on the image quality, and *no water retrieval* was conducted because no specific band was configured with the Landsat instruments. After carrying out the atmospheric correction, radiance values were converted into surface reflectance (ρ_w) [30] which was further converted to remote sensing reflectance (R_{rs}) by dividing pi (π):

$$R_{rs} = \rho_w / \pi \quad (4)$$

Once the image is calibrated as R_{rs} , it is possible to apply directly the relationship between turbidity and R_{rs} computed with a training set of in situ point data to obtain a gridded image of turbidity [32]. In the current study, R_{rs} was used to develop turbidity model.

2.5.4. Regression Models

Using preprocessed satellite images, it is possible to identify which band's reflectance showing the most significant regression with turbidity. To avoid non-water features such as artificial structures (bridges) or eliminate distortion as well as disturbances, the pixel data within a 90-m distance (3×3 pixels) from structures were excluded from the analysis [33,34]. The average values of 3×3 pixels were extracted for statistical analyses by defining a region of interest (ROI) corresponding to that specific area. These ROIs were created as rectangles corresponding to the stations measured in the field.

Subsequently, simple linear regressions were exploited to develop a relation between in situ measurements and the space-based observations. Ritchie et al. developed algorithms for remote sensing retrieving water quality parameters, including suspended solids [35]. The general forms of these empirical equations were given by the following four types of expressions:

$$\begin{aligned} Y &= A + BX \\ Y &= AB^X \\ Y &= A + B \ln X \\ \ln Y &= A + BX \end{aligned} \quad (5)$$

where X is the remote sensing measurement (i.e., radiance, reflectance, and energy) and Y is the water quality parameter of interest (i.e., suspended sediment, and chlorophyll). A and B are empirically derived factors and X could be reflectance, radiance, energy in a single band, or ratio of two bands. Most of the studies on remote sensing for retrieving water quality parameters have adopted this concept, which was also followed by the present study to develop an algorithm for turbidity retrieval based on the correlation between remote sensing reflectance and in situ turbidity.

2.6. Numerical Estimation of Bed Shear Stress

To discuss the effect of waves on resuspension of sediment and the resultant increase in turbidity, spatiotemporal bed shear stresses were estimated by combining numerical wave hindcasting using SWAN and the linear water wave theory.

2.7. Numerical Hindcasting of Wave Field Using SWAN

SWAN (Simulating WAVes Nearshore) model developed by Delft University of Technology, the Netherlands, is a third-generation, discrete spectral wave model that describes the evolution of the two-dimensional wave energy spectrum in arbitrary conditions of wind, currents, and

bathymetry [36,37]. This model has been widely used in communities of coastal engineering and physical oceanography. The governing equation is given by:

$$\frac{\partial N}{\partial t} + \frac{\partial C_x N}{\partial x} + \frac{\partial C_y N}{\partial y} + \frac{\partial C_\sigma N}{\partial \sigma} + \frac{\partial C_\theta N}{\partial \theta} = \frac{S}{\sigma} \quad (6)$$

where $N(\sigma, \theta; x, y, t)$ is the action density as a function of the intrinsic frequency σ , the wave direction θ , the horizontal coordinates of x and y , and the time t . The action density is defined as $N = E/\sigma$ using the energy density E . The first term on the left-hand side represents the local rate of change of action density in time, the second and third terms represent propagation of action in geographical (x, y) coordinates with the wave celerities of C_x and C_y . The fourth term denotes the shifting of the relative frequency due to variations in depths and currents and the fifth term represents depth and current-induced refraction. The source term $S(\sigma, \theta; x, y, t)$ on the right-hand side represents the generation, dissipation and non-linear wave-wave interactions [36].

Estimation of Bed Shear Stress

There are various models for predicting wave induced or combined wave and current induced bed shear stress [38]. In Cam Ranh Bay and Thuy Trieu Lagoon, the magnitudes of typical tide induced currents in dry and rainy seasons are 0.15 m/s and 0.25 m/s, respectively [39]. Considering these small current velocities and shallow water bodies, the bed shear stress due to wind waves can be much larger than that due to currents [2], and thus only the wave induced stress was included in this study. The maximum bed shear stress τ_{bm} is estimated by:

$$\tau_{bm} = \frac{1}{2} \rho f u_{bm}^2 \quad (7)$$

where ρ and f are the water density and the friction factor, respectively, and u_{bm} is the amplitude of the wave induced orbital velocity at the bottom determined by [40]:

$$u_{bm} = \frac{\pi H_s}{T_p \sinh(2\pi h/L)} \quad (8)$$

using the small amplitude water wave theory, where h is the water depth, H_s , T_p and L are the significant wave height, the peak wave period and the wavelength, respectively, obtained from the SWAN computation.

In the present study, owing to the lack of data on wave field and bottom roughness in the study site, f is assumed to have a constant value of 0.004 [41]. The description of adopted model parameters and computational conditions is presented in Table 3.

Table 3. Description of computational conditions for SWAN (Simulating WAVes Nearshore) model.

Input Parameters	Input Values/Command
(a) Details of computational grid and input bottom grid	
Computational Grid	Regular and uniform
Origin (E, N), direction of positive x-axis of computational grid	292022.3 1306301 0. (the original grid cell on the lowest left corner/UTM)
Length of computational grid (x, y)	16315 m, 33735m
Number of meshes (x, y)	251, 520
Spectral direction	Circle
Number of mesh in θ space	36
Discrete frequency (lowest, highest)	0.05 Hz, 1 Hz
Grid resolution in frequency-space	31
Bottom Grid (input file)	Regular and Uniform
Number of meshes (x, y)	251, 520
$\Delta x, \Delta y$ (grid resolution)	65 m, 65 m
(b) Details of boundary condition	
Boundary spectral shape	JONSWAP as default
Gamma	3.3—peak enhancement parameter of JONSWAP spectrum
Peak	Peak Period. This is default
DSPR	Expressing the width of the directional distribution
Power	The directional width is expressed with the power m itself, this option is default
Initial Values for Stationary computation	Zero (0), The initial spectral densities are all 0
(c) Physical processes employed	
Wave-generation mode	GEN3 Komen
Whitecapping	Calculation based on Komen
Computation of quadruplet wave interaction	Iquad = 2 (default)
Breaking	Constant with $\alpha = 1$ and γ (breaker index) = 0.73 (default)
Bottom friction	Activated using JONSWAP formulation, Friction coefficient: constant ($0.067 \text{ m}^2 \text{ s}^{-3}$)
Triad	To activate the triad wave-wave interactions
Wave limiter	Activated; upper threshold = 10.0; Threshold for fraction of breaking waves = 1.0

3. Results

3.1. Field Observation and Collected Data

Analyses of Water Sample

Measured mean, minimum and maximum values for Total, Organic, and Inorganic Suspended Solids (TSS, OSS and ISS, respectively), and chlorophyll-a concentrations (Chl-a) are presented in Table 4 along with the ratios of OSS/TSS and ISS/TSS in September 2015 (rainy season) and in February 2016 (dry season). Turbidity is also shown in February 2016 in FTU (Formazine Turbidity Unit).

Table 4. Mean, minimum and maximum values of water quality variables in (a) rainy season (September 2015) and (b) dry season (February 2016).

(a) In Rainy Season (September 2015)							
	TSS (mg/L)	OSS (mg/L)	ISS (mg/L)	Chl-a ($\mu\text{g/L}$)		OSS/TSS	ISS/TSS
Mean	5.96	2.09	3.87	5.34		0.43	0.57
Min.	0.95	0.55	0.15	0.81		0.21	0.16
Max.	25.70	7.30	18.40	13.77		0.84	0.79
(b) In Dry Season (February 2016)							
	TSS(mg/L)	OSS (mg/L)	ISS (mg/L)	Chl-a ($\mu\text{g/L}$)	Turbidity (FTU)	OSS/TSS	ISS/TSS
Mean	7.82	3.80	4.01	20.79	1.41	0.46	0.54
Min.	1.75	0.80	0.60	1.56	0.21	0.22	0.20
Max.	52.00	31.11	20.89	266.01	3.46	0.80	0.78

At the top of the lagoon with very shallow waters of around 0.5 to 1.5 m deep (Figure 1), Chl-a concentrations were higher than those at other stations in deep waters while TSS were low. In both rainy and dry seasons, the ratios of ISS/TSS were slightly higher than OSS/TSS on average and thus the contributions of inorganic substances, such as sand, silt or clay particles, and organic matters are nearly equal. This result revealed that the influence of algae was significant to spectral reflectance of the study area.

3.2. Turbidity Retrieval

Following the concept of Ritchie et al. (2003), linear regression models for turbidity were developed using the remote sensing reflectance extracted from Landsat 8 OLI on 14 February 2016 and observed turbidity in February 2016, as shown in Table 5. It can be seen that the lowest R^2 is 0.07 for the model No. 10 using the ratio of B5/B3 as the regression parameter while the highest R^2 is 0.84 for the model No. 1 adopting the single Band 4 (B4) (red region) (Figure 3). Selecting Band 4 as the regression parameter, the regression model for turbidity was determined as:

$$\text{Turbidity} = 380.32R_{rs}(\lambda_{B4}) - 1.7826 \tag{9}$$

where λ_{B4} is the wavelength of Band 4 (B4).

Table 5. Regression models for turbidity retrieval (B1 = 433 nm, B2 = 482 nm, B3 = 562 nm, B4 = 655 nm and B5 = 865 nm).

No.	Regression Models	R^2	Significant
1	Turbidity = $380.32 \times R_{rs} (B4) - 1.7826$	$R^2 = 0.84$	$p < 0.05$
2	Turbidity = $-8.1043 \times R_{rs} (B5/B4) + 7.2697$	$R^2 = 0.79$	$p < 0.05$
3	Turbidity = $297.86 \times R_{rs} (B3) - 2.8208$	$R^2 = 0.70$	$p < 0.05$
4	Turbidity = $604.54 \times R_{rs} (B5) - 2.2241$	$R^2 = 0.48$	$p < 0.05$
5	Turbidity = $424.54 \times R_{rs} (B2) - 4.4504$	$R^2 = 0.45$	$p < 0.05$
6	Turbidity = $504.31 \times R_{rs} (B1) - 7.1769$	$R^2 = 0.42$	$p < 0.05$
7	Turbidity = $12.895 \times R_{rs} (B5/B1) - 3.158$	$R^2 = 0.37$	$p < 0.05$
8	Turbidity = $6.3388 \times R_{rs} (B4/B3) - 2.4028$	$R^2 = 0.35$	$p < 0.05$
9	Turbidity = $5.5354 \times R_{rs} (B5/B2) - 1.0947$	$R^2 = 0.13$	$p < 0.05$
10	Turbidity = $3.5623 \times R_{rs} (B5/B3) + 2.8059$	$R^2 = 0.07$	$p < 0.05$

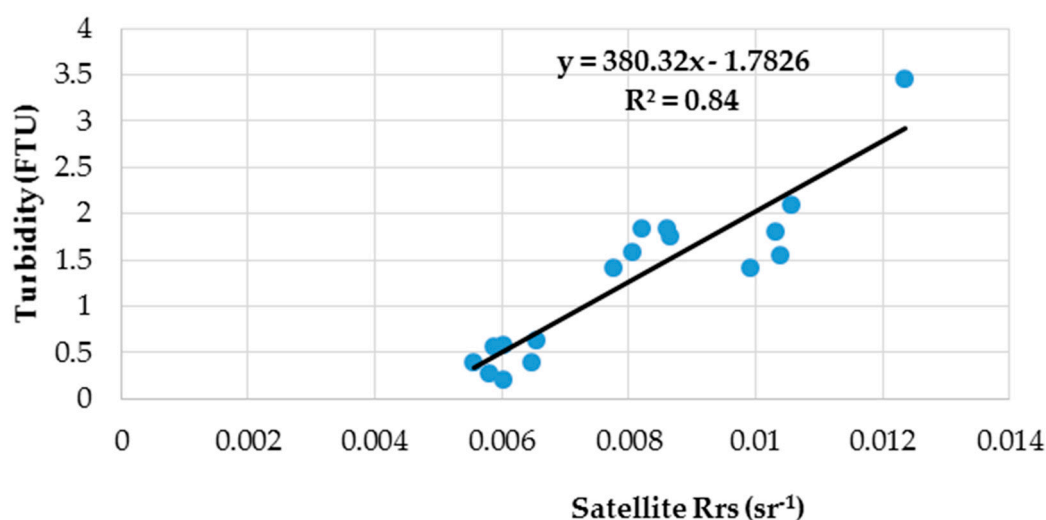


Figure 3. Correlation between remote sensing reflectance at 655 nm extracted from Landsat 8 OLI on 14 February 2016 and turbidity from in situ by using AAQ sensor.

A comparison of turbidities between computed using Equation (9) and observed at 17 stations (see Figure 1 and observed data missing at Station 11) is shown in Figure 4 and Table 6 along with squared residual, root mean square error (RMSE) and scatter index (SI), which shows a high correlation factor ($R^2 = 0.84$). The root mean square error (0.28) and scatter index (0.22) are low and acceptable [15,42]. The retrieved turbidities using Landsat 8 OLI are thus consistent with measured turbidities. These results indicate that the proposed model could be used to retrieve turbidity in highly turbid waters in the bay and lagoon.

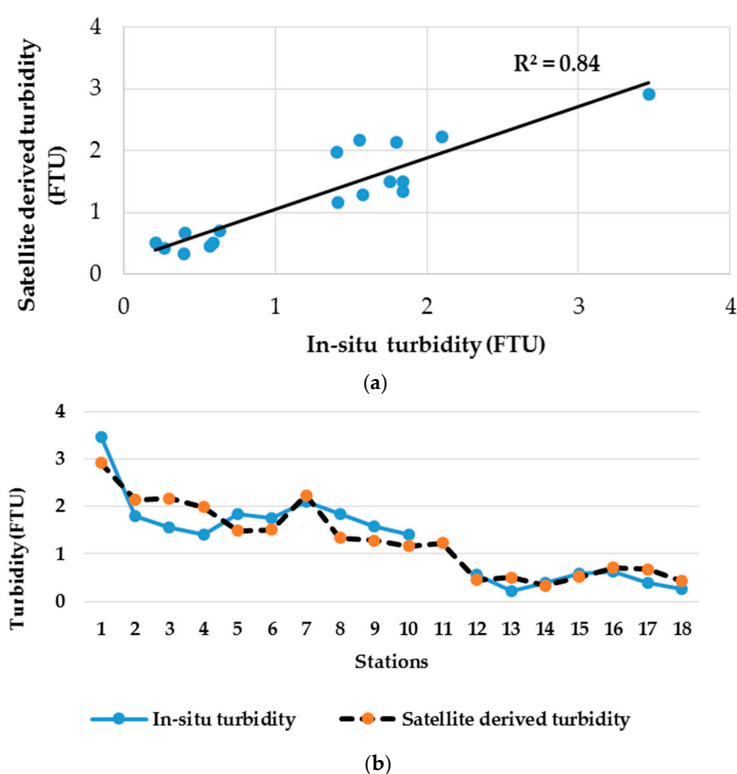


Figure 4. Scatter plots (a) and line graphs (b) comparing between satellite retrieved and observed turbidities at 18 stations shown in Figure 1 (observed turbidity missing at Station 11).

Table 6. Comparison of observed and retrieved turbidities with statistical analyses for squared residual, root mean square (RMSE) and scatter index (SI) from Station 1 to Station 18 except Station 11 in Figure 1.

Stations	Turbidity Observed	Turbidity Computed	Squared Residual	RMSE	SI
Station 1	3.46	2.92	0.30		
Station 2	1.80	2.14	0.12		
Station 3	1.56	2.17	0.37		
Station 4	1.41	1.99	0.33		
Station 5	1.84	1.49	0.12		
Station 6	1.76	1.51	0.06		
Station 7	2.10	2.23	0.02		
Station 8	1.85	1.33	0.26		
Station 9	1.58	1.28	0.09	0.28	0.22
Station 10	1.41	1.17	0.06		
Station 12	0.57	0.45	0.02		
Station 13	0.21	0.50	0.08		
Station 14	0.40	0.33	0.01		
Station 15	0.60	0.51	0.01		
Station 16	0.63	0.71	0.01		
Station 17	0.40	0.68	0.07		
Station 18	0.27	0.43	0.03		

3.3. Spatio-Temporal Variation in Turbidity

Using Equation (9), spatial variation in turbidity was retrieved for each of the collected Landsat 8 OLI images summarized in Table 2 from 29 June 2013 to 14 February 2016, and classified into rainy season, dry season and shortly after rainfall in dry season, respectively. By retrieving turbidities from pixels of the Landsat 8 OLI images, the relationship between turbidity and its frequency was obtained in rainy season, dry season and shortly after rainfall in dry season, as shown in Figure 5.

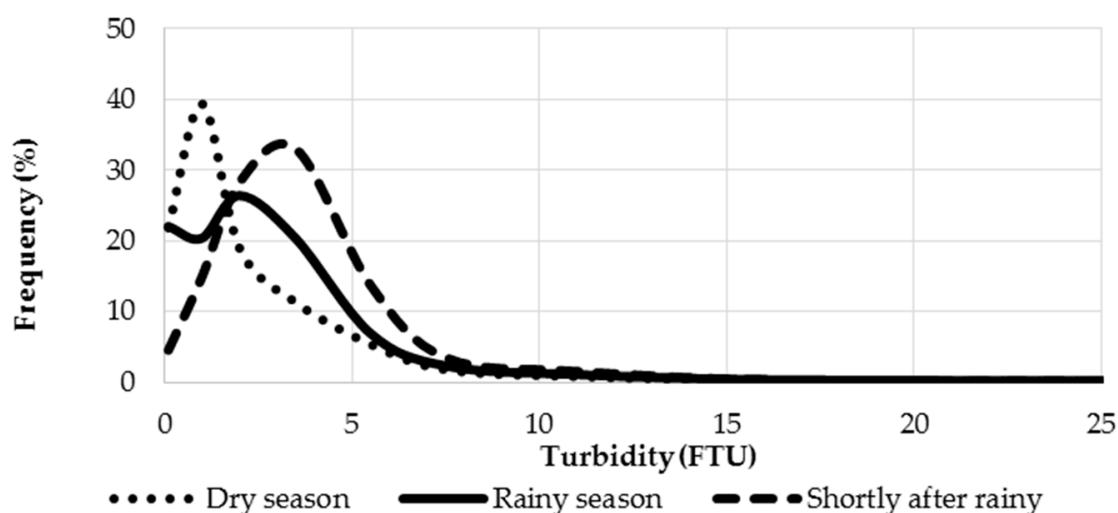


Figure 5. Frequency distribution of mean turbidity retrieved from Landsat 8 OLI images from 2013 to 2016 using the empirical model of Equation (9) in rainy season (four scenes), dry season (six scenes), and shortly after rainfall in dry season (eight scenes).

Turbidities ranging from 2.5 to 3.5 FTU were the most frequent values in rainy season (9 October 2015) with the highest frequency of 40%. Similarly, shortly after rainfall in dry season, turbidities around 3.5 FTU were the dominant values with the highest frequency of 55.8% (16 August 2013). By contrast, the most frequent values of turbidity in dry season were around 1.0 FTU with the frequency of 34% (26 January 2015).

3.4. Turbidity Distribution in Dry Season

Spatial variations in retrieved turbidity in dry season (on 8 February 2014, 2 July 2014, 26 January 2015, 15 March 2015, 3 June 2015 and 14 February 2016) are shown in Figure 6. Generally, turbidity is low in dry season except in shallow waters and areas adjacent to the coastlines. There are insignificant fluctuations of the mean turbidities ranging from 1.09 to 1.51 FTU during dry season. Small amount of precipitations less than cumulative 150 mm for ten-day period were recorded for these days. It is worth noting that rain rarely occurs during the dry season and almost no water flows in the rivers. High turbidity appearing near the river mouths and near shorelines might be due to resuspension of bed sediment.

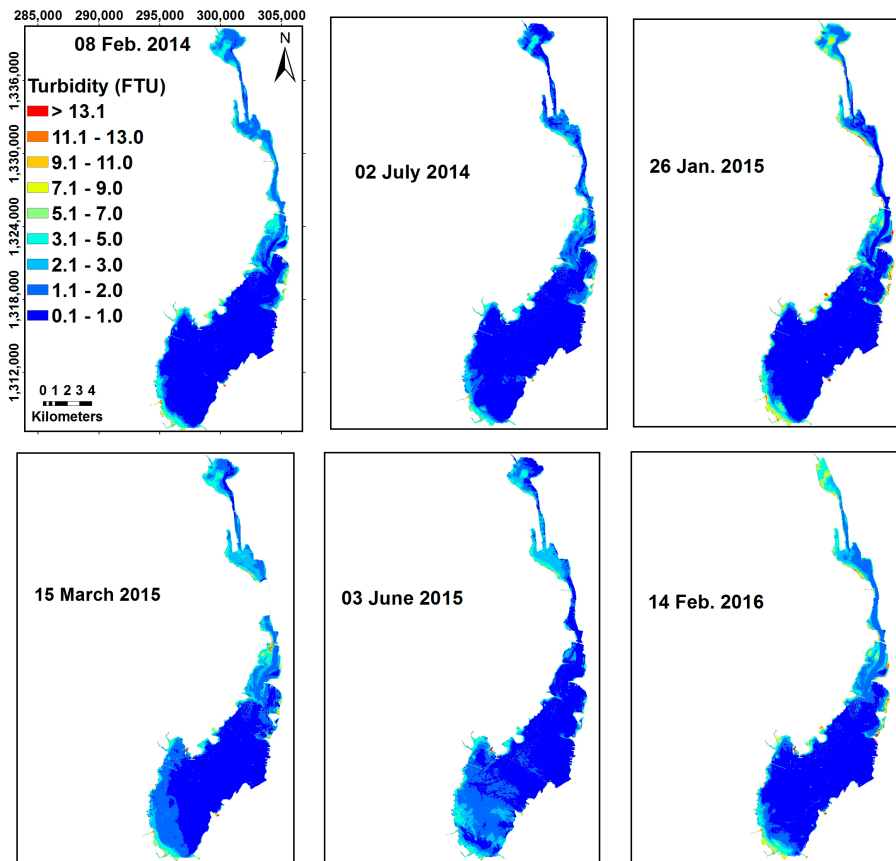


Figure 6. Turbidity distributions in dry season (cloud cover areas masked).

3.5. Turbidity Distribution in Rainy Season

Spatial variations in retrieved turbidity in rainy season (on 20 September 2014, 7 September 2015, 23 September 2015 and 9 October 2015) are shown in Figure 7. Compared with in dry season, the mean turbidities in rainy season were slightly higher (Table 6), notably in deep waters in Cam Ranh Bay. Both patterns in rainy and dry seasons show high turbidity in shallow water areas adjacent to coastlines. Turbidity in rainy season is slightly higher around the bay mouth than that in dry season. Depending on the amount of precipitation, the pattern as well as concentration of turbidity changed. The relationship between rainfall and turbidity will be further discussed in the section of discussion.

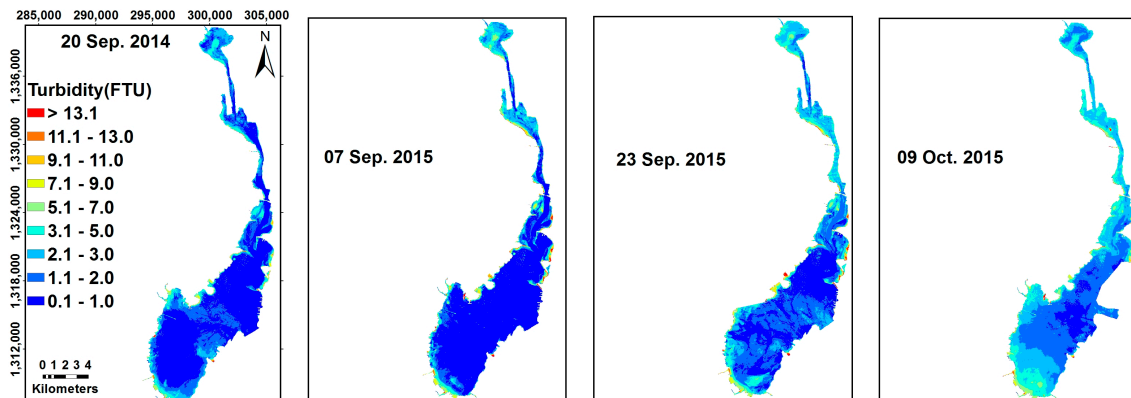


Figure 7. Turbidity distributions in rainy season (cloud cover areas masked).

3.6. Turbidity Distribution in Shortly after Raining in Dry Season

Spatial variations in retrieved turbidity shortly after rainfall in dry season (on 29 June 2013, 16 August 2013, 12 March 2014, 15 May 2014, 16 April 2015, 21 July 2015, 6 August 2015 and 22 August 2015) are shown in Figure 8. River discharges into the bay and lagoon are controlled by dams in their up streams and thus after heavy rain, waters are impounded in the reservoirs first [38]. Turbidities in the river mouths therefore do not immediately become high after rainfall and strongly depend on the operation of the dams. Similar to the turbidity patterns in dry and rainy seasons, high turbidities appear in shallow water areas adjacent to the coastlines. This reason might be due to resuspension of bed sediment. After rainfall, high turbidities appear not only in shallow water areas in the river mouths but also in deep waters where turbid waters discharging from the rivers could penetrate far offshore in the bay (Figure 8).

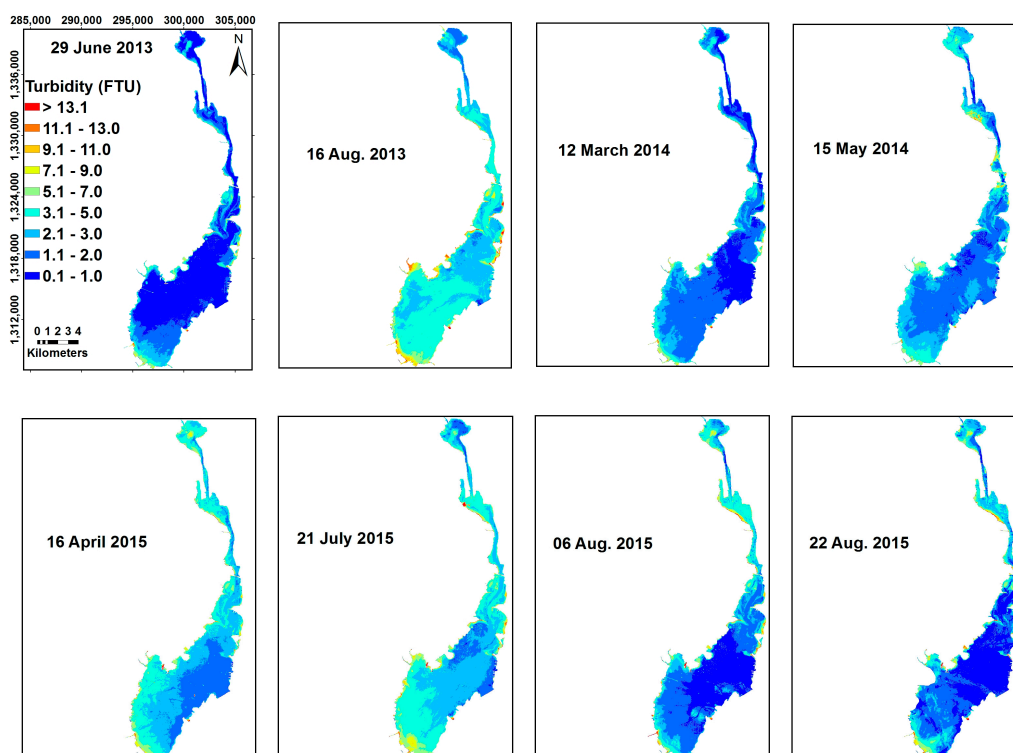


Figure 8. Turbidity distributions shortly after rainfall in dry season (cloud cover areas masked).

3.7. Statistics of Retrieved Turbidities

A statistical summary of turbidities in dry season, rainy season and shortly after rainfall in dry season retrieved from the 18 images is shown in Table 7. A wide range of turbidity was seen from 0.01 to 68.89 FTU. Turbidities in dry season ranged from 0.01 to 68.89 FTU with their mean values from 1.02 to 1.51 (see Table 7 and Figure 5). In rainy season, turbidities ranged from 0.01 to 46.64 FTU with their mean values from 1.18 to 2.35 FTU (see Table 7 and Figure 5). Shortly after rainfall in dry season, turbidities ranged from 0.01 to 44.2 FTU with their mean values from 1.29 to 3.68 FTU (see Table 7 and Figure 5).

Table 7. Statistics of seasonal variation in turbidities across the bay and lagoon retrieved from Landsat 8 OLI images from 2013 to 2016.

Seasons	Time	Max.	Min.	Median	Mean	Std.
Dry	8 February 2014	22.28	0.01	0.30	1.09	1.52
	2 July 2014	22.93	0.01	0.54	1.02	1.26
	26 January 2015	42.42	0.01	0.32	1.29	2.10
	15 March 2015	68.89	0.01	0.89	1.29	1.65
	3 June 2015	50.66	0.01	0.92	1.24	1.56
	14 February 2016	48.37	0.01	0.71	1.51	2.05
Rainy	20 September 2014	27.50	0.01	0.68	1.18	1.47
	7 September 2015	46.64	0.01	0.10	1.20	2.19
	23 September 2015	40.24	0.01	1.46	1.90	1.92
	9 October 2015	37.38	0.02	2.04	2.35	1.58
Shortly after rainfall during dry season	29 June 2013	19.69	0.01	0.83	1.29	1.39
	16 August 2013	23.17	0.10	3.27	3.68	1.62
	12 March 2014	21.92	0.01	1.39	1.76	1.26
	15 May 2014	19.16	0.01	1.91	2.29	1.32
	16 April 2015	39.78	0.10	2.64	2.96	1.50
	21 July 2015	42.34	0.01	2.93	3.35	1.73
	6 August 2015	42.47	0.01	1.49	2.06	1.97
	22 August 2015	44.20	0.01	1.37	1.88	2.11

Figure 9 shows the mean turbidities extracted from 18 Landsat 8 OLI scenes. It also reveals that the turbidity had significant temporal variability between 2013 and 2016. In dry season, mean turbidity ranged from 1.0 to 1.5 FTU and slightly higher in rainy season from 1.2 to 2.3 FTU. The highest fluctuation occurred shortly after rainfall from 1.3 to 3.7 FTU.

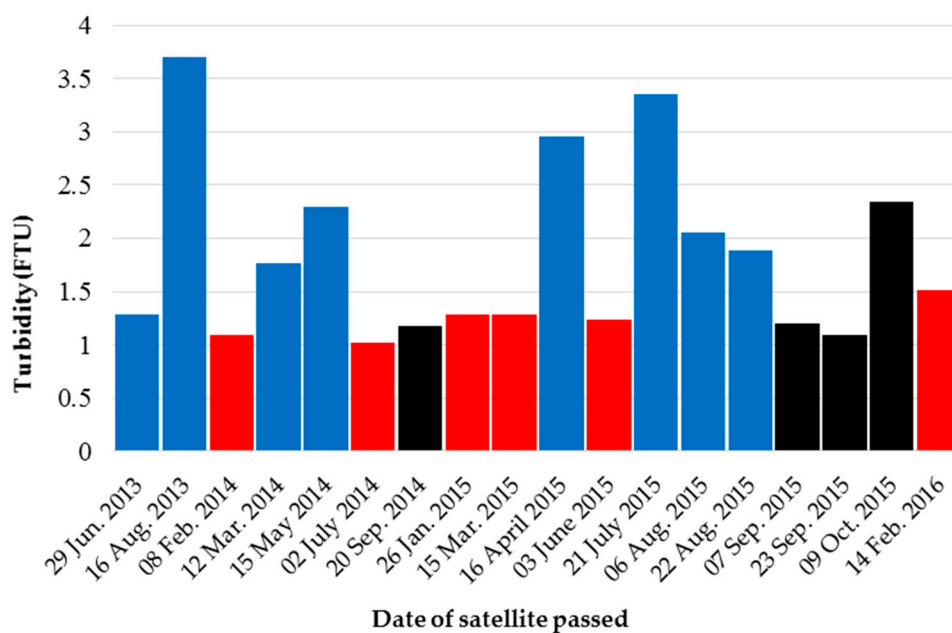


Figure 9. Landsat 8 OLI extracted mean turbidities in Cam Ranh Bay and Thuy Trieu Lagoon from 2013 to 2016 in both dry and rainy seasons (blue for shortly after rainfall in dry season, red and black for dry and rainy seasons, respectively).

3.8. Distribution of Wave Characteristics and Bed Shear Stress

In this study, wind was considered the most important input data for SWAN simulation because waves were mainly induced by wind. Due to the lack of measured significant wave height data, only observed wind was used to verify the input files. A comparison between observed wind provided by Institute of Oceanography and estimated data from NCEP FNL at 10 m height is presented in Figure 10.

The average observed and estimated wind speeds were 6.77 and 6.55, respectively. RMSE (2.39) and SI (0.35) values were small. These results showed high consistency between observed and estimated wind speed. Based on those, wind speed downloaded from NCEP FNL was appropriate and could be used in this study with high precision.

To estimate typical variations in significant wave heights and wave induced bed shear stresses across Cam Ranh Bay and Thuy Trieu Lagoon in dry season (northeast monsoon) and rainy season (southwest monsoon), respectively, SWAN model was forced by northeast (NE) winds and southwest (SW) winds with wind speeds at 1, 3, 5, 7, 9, 11 and 13 m/s which were chosen based on the statistics of wind fields in the study site extracted from the NCEP FNL dataset from 1999 to 2015. Figures 11 and 12 show computed significant wave heights and wave induced bed shear stresses in dry season and rainy season, respectively.

During rainy season (SW monsoon), the bed shear stress is higher in SW monsoon than in NE monsoon when wind speed was greater than 5 m/s in shallow waters, the top of Thuy Trieu Lagoon. However, in deep waters, Cam Ranh Bay, wind speed less than 9 m/s did not generate high bed shear stresses. The results at the central part of the study area were the most sensitive to change in wind speed. When wind speed was greater than 9 m/s, almost the entire study area had high bed shear stress.

The variations of significant wave height and bed shear stress to different wind speeds in NE monsoon (rainy season) were shown in Figure 12. Wind speeds greater than 5 m/s could generate a large area of high bed shear stresses leading to resuspension of sediments during NE monsoon. In deep waters, resuspension of sediments might occur when wind speeds were greater than 9 m/s. When wind speed reached 13 m/s, most of the study area showed high bed shear stresses including deep waters in Cam Ranh Bay (see Figures 11a and 12a).

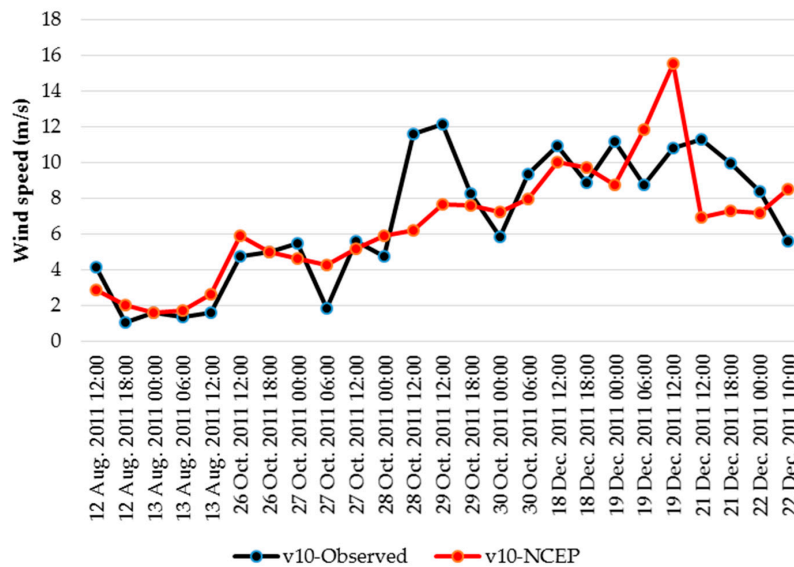


Figure 10. Comparison between observed and estimated (NCEP) wind speeds at 10 m height.

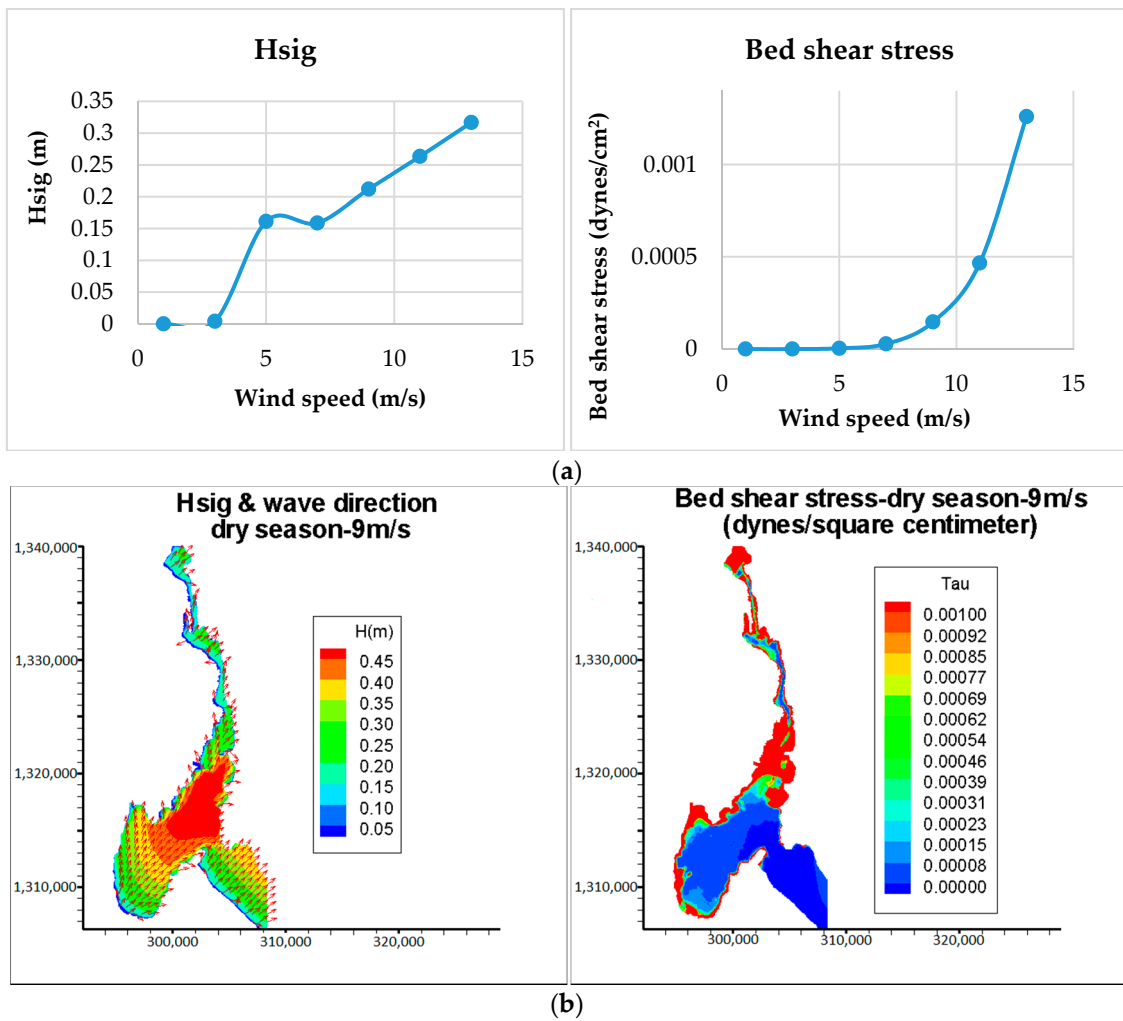


Figure 11. Typical variations of significant wave heights and directions as well as bed shear stresses in dry season (NE monsoon, -45 degree). Top panels (a) show relationships between wind speeds and significant wave heights and bed shear stresses, respectively, at 296,437.06 lat. 1,308,613.36 long. and bottom panels (b) show spatial distributions with the wind speed of 9 m/s.

Aside from the dependence on wind speed, the sensitivity of significant wave height and bed shear stress to different wind directions were analyzed. Wind speed ranging from 5 to 9 m/s was dominant in the period from 1999 to 2015 based on the wind analysis of NCEP FNL. Moreover, NE and SW are the main directions of wind in dry and rainy seasons, respectively. Based on those, wind speed at 7 m/s was used as a representative to assess the sensitivity of wave spectrum to wind direction for every 10 degree interval.

According to Figure 13, the amount of resuspension was influenced not only by wind speed, but also by wind direction. The simulation results showed that SW winds caused less resuspension than NE winds in deep waters, Cam Ranh Bay. In the upper part of Thuy Trieu Lagoon and the center of the study area, shallow waters had much influence on resuspension in both SW and NE monsoon. At the bay mouth, where the water depth is around 30 m, the bed shear stress was always small and approximately 0 in both NE and SW monsoon.

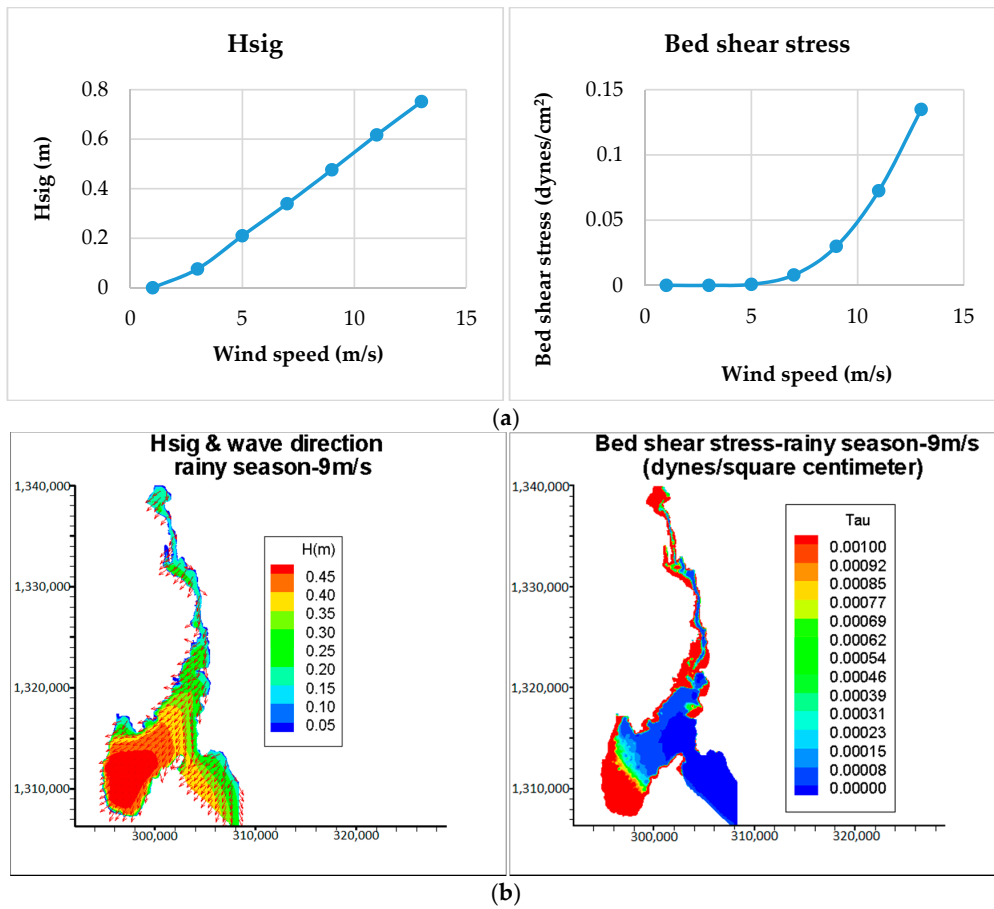


Figure 12. Typical variations of significant wave heights and directions as well as bed shear stresses in rainy season (SW monsoon, -225 degree). Top panels (a) show relationships between wind speeds and significant wave heights and bed shear stresses, respectively, at 296,437.06 lat. 1,308,613.36 long. and bottom panels (b) show spatial distributions with the wind speed of 9 m/s.

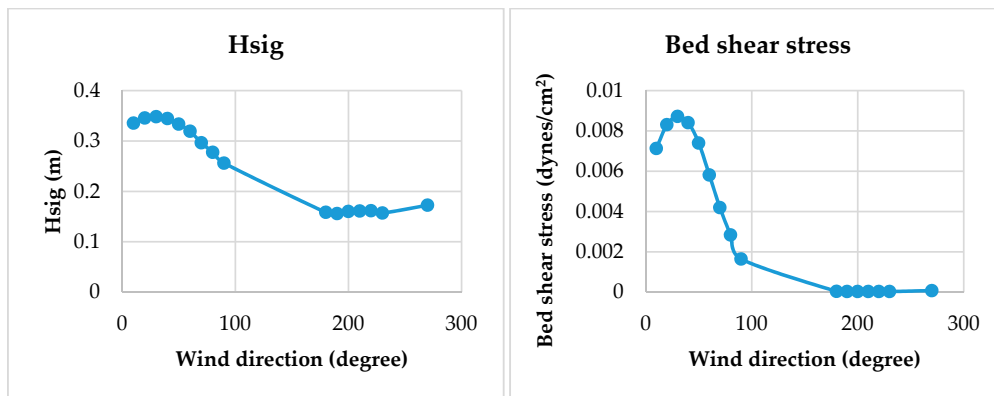


Figure 13. Variations of significant wave height and bed shear stress to different wind directions (at station 296,437.06 lat. 1,308,613.36 long.) in NE and SW monsoons.

4. Discussion

4.1. Turbidity Algorithm

Most of the existing methods interpreting turbidity propose site-specific empirical relationships between turbidity and reflectance at different satellite wavebands by fitting field turbidity measurements

with either field- or satellite-derived reflectance [7]. Single band or ratio of two bands is routinely used to develop turbidity as well as other water component models [32,35]. In the present study, turbidity showed the highest correlation with Band 4 of Landsat 8 OLI, red region (655 nm) for a single season.

The best fit of the red band to characterize the turbidity of Cam Ranh waters is not surprising. Many researchers using remote sensing reflectance (R_{rs}) for turbidity as well as TSS retrieval have shown that there is high relationship between red band of satellite images and their concentrations. Güttler et al. [1] developed an algorithm for turbidity in the Northwestern Black Sea coastal zone based on the high correlation between turbidity and red band of Landsat TM. Lobo et al. used a time-series analysis of Landsat-MSS/TM/OLI images to assess the impacts of gold mining activities to Amazonian waters. This result indicated that water reflectance of red band of Landsat was the most appropriate for establishing a robust empirical model for TSS retrieval [43]. Vanhellemont and Ruddick used Landsat 8 OLI Band 4 to retrieve turbidity in the Southern North Sea where the water depth was less than 50 m. They also used MODIS red band, 645 nm, for testing turbidity retrieval algorithm. The results showed that red region was appropriate for interpret turbidity from satellite images [11]. In addition, Garaba and Zielinski were successful in using Landsat 8 OLI to interpret turbidity in estuary located in Wadden Sea where turbidity was always high. The result revealed that turbidity highly correlated with remote sensing reflectance Band 4, red region, of Landsat 8 OLI [44].

In low turbid waters where total suspended solids (TSS) are less than 50 g/m^3 , there is high correlation between turbidity and remote sensing reflectance of red region [6]. However, for waters with very high turbidity or TSS exceeding 50 mg/m^3 , near infrared (NIR) wavelengths are recommended to use for turbidity retrieval [6]. The shift to NIR wavelength for turbidity retrieval is due to the saturation of R_{rs} in visible wavelengths when TSS concentration exceeds 50 g/m^3 [6,45]. These results also indicated that, in very turbid waters where TSS exceeds 100 g/m^3 , the R_{rs} signal in the short-wavelength infrared region (SWIR, 1000–3000 nm) could also be used to retrieve turbidity and inherent optical properties [6,46]. The sensitivity of remote-sensing reflectance to turbidity was inversely related to suspended sediment concentration [45]. This study also indicated that NIR wavelength should be used to retrieve suspended sediment matter for the very high turbid waters.

In our study, the TSS measured in two field trips were less than 20 mg/L except station 14 where algae blooming occurred (52 mg/L and slightly higher than 50 mg/L , the threshold). Therefore, the algorithm that was developed for turbidity retrieval was stable and reliable when using red band.

Notably, the algorithm developed from in situ R_{rs} data and then applied to Landsat-based on derived R_{rs} data with a spectral response function for satellite images can result in errors or uncertainty of the model [47]. The reason of this uncertainty is due to the differences of spectral reflectance between R_{rs} measured and calculated from the images. They cannot be exactly the same, even though satellite images are undergone rigorous calibrations. For adopting the spectra for Landsat sensors, the derived-turbidity model is the best precision with the highest determination coefficient ($R^2 = 0.84$; $p < 0.05$), using only one red band available from the entire Landsat satellite [47]. Furthermore, there is no difference in the spatial and spectral resolution of all 18 satellite images because only Landsat 8 OLI was used. In other words, the turbidity algorithm can be applied for all the Landsat 8 OLI images without uncertainty.

4.2. Factors and Processes Determining Turbidity

In order to discuss factors and processes determining turbidity, a correlation between measured sediment grain size and estimated turbidity has firstly been investigated as shown in Figure 14 representing a negative weak correlation between turbidity and median sediment diameter (d_{50}) in the bay and lagoon. This correlation is similar to that in a study by Richardson and Jowett (2002), which also showed a similar negative weak correlation ($R = -0.34$) [48]. These results indicate the easier occurrence of wave induced resuspension of finer sediment leading to higher turbidity while the correlation factor is not very high, which means turbidity is also influenced by other factors, including the relationship between bed shear stress and sediment properties and the effect of turbid water

discharges and dispersion during floods as well as the influence of clear oceanic water intrusions through the bay entrance leading to lower turbidity.

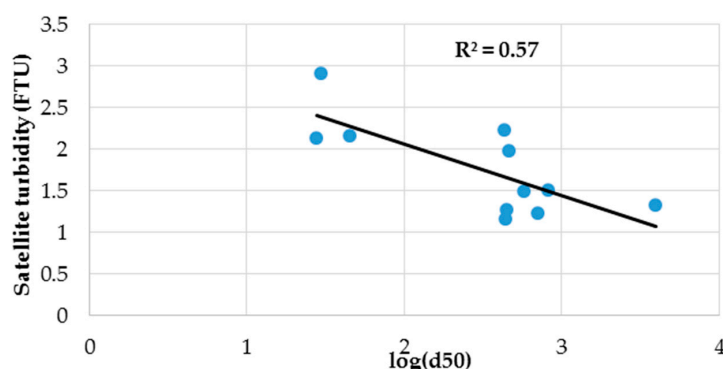


Figure 14. Correlation between Landsat 8 OLI extracted turbidities and $\log(d_{50})$.

During the dry season, low turbidity waters appeared in most of the study areas except shallow waters and areas adjacent to coastlines. Turbidity in Thuy Trieu Lagoon was always slightly higher than in Cam Ranh Bay (see Figures 6–8), especially in the central part of the lagoon, while, around the bay mouth, turbidities were in the range from 0.1 to 1.0 FTU and lower than in the lagoon. These higher turbidities are considered to be mainly caused by wave induced resuspension of bed sediments in shallow waters, which is confirmed by the appearance of higher turbidity areas corresponding to shallower water areas, as bed shear stress tends to decrease with increasing water depth [32]. By extracting and averaging bed shear stresses (BSS) from each of Landsat scenes, correlations were taken between BSS and turbidities under small rainfall and heavy rainfall conditions, respectively, as shown in Figure 15.

Figure 15a indicates that the variation of turbidity was mainly governed by resuspension of bed sediments under small rainfall conditions. However, under heavy rainfall conditions, relationship between bed shear stress and turbidity became insignificant, as shown in Figure 15b, which will be discussed later. Under calm weather conditions, the amount of fresh water discharges into the bay and lagoon are basically small due to being controlled by the dams and thus no significant sediment supply occurs from the rivers [10]. Wind speed under calm weather conditions is not high enough to generate shear zones leading to high turbidity even in deep waters in Cam Ranh Bay. According to the results from SWAN simulation, winds with the speed of less than 9 m/s were not a major factor causing higher turbidity in deep waters (see Figure 12). This result may be in favor of that of a previous case study in China [47].

SWAN simulation results also showed that only wind speeds greater than or equal to 9 m/s could generate high bed shear stress areas leading to resuspension of bed sediments in deep waters of Cam Ranh Bay (see Figures 11 and 12). However, for the closed water areas like Cam Ranh Bay and Thuy Trieu Lagoon, wind speed usually less than 9 m/s. The combination of high wind speed with large amount of precipitation will result in high turbidity during NE monsoon. Besides, the wave heights are associated with the fetch dependent on the shape of the study area and the wind direction. Higher waves were found at the head of the lagoon during SW monsoon and at the southern part of the bay and areas adjacent to the coastlines in NE monsoon (Figures 11b and 12b), as these two areas are the downwind regions in SW and NE monsoons, respectively.

To see the relationship between turbidity and the amount of precipitation from 2013 to 2016, retrieved turbidities and the corresponding cumulative rainfalls during ten days before taking each of the images are plotted in the top panel of Figure 16a and their correlation is shown in Figure 16b. Among a variety of factors affecting turbidity, its correlation factor of $R^2 (= 0.54, p < 0.05, t\text{-test})$ is considerably high [15,49] and thus these rainfall events are considered as a major contributor for increasing in turbidity through a large amount of river discharges with high turbidity.

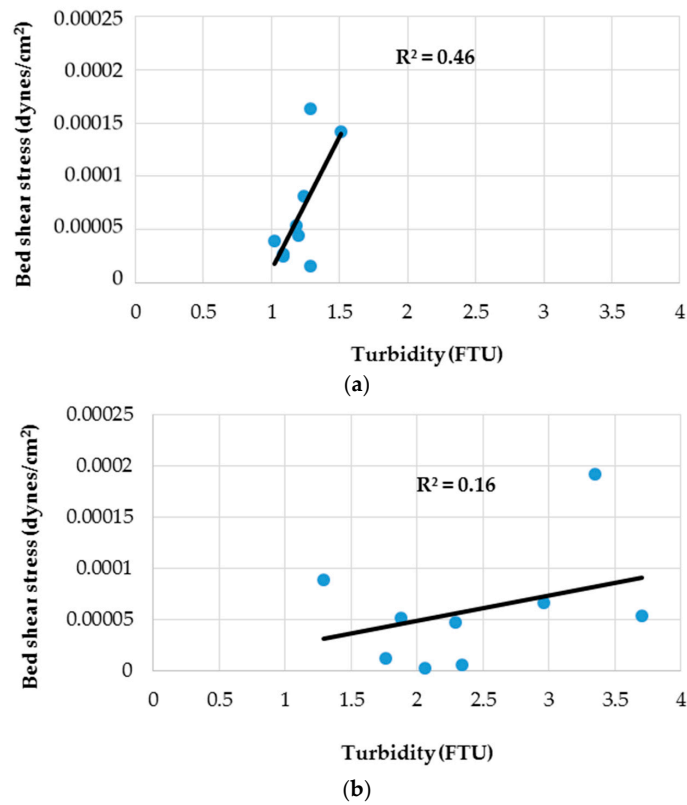


Figure 15. Correlation between the mean Landsat OLI extracted turbidities and computed bed shear stresses under (a) small rainfall condition and (b) heavy rainfall condition.

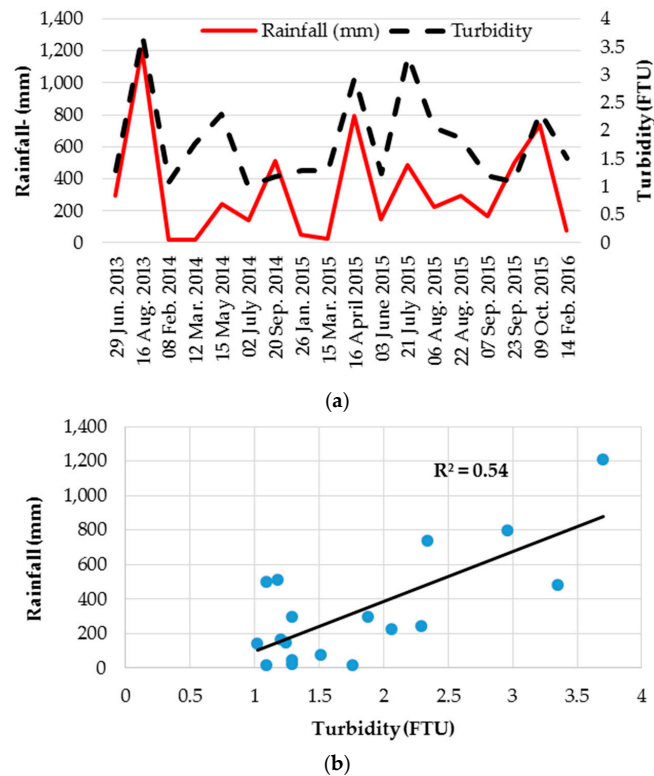


Figure 16. (a) Time series of measured rainfalls and the mean Landsat 8 OLI extracted turbidities and (b) their correlation.

According to Figure 16, turbidity in the bay contributed from the rivers was strongly influenced by a large amount of precipitation through the two main processes: (i) after rainfall, the river runoff bringing a large amount of sediment into the river mouths, which is expected to increase the concentration of suspended sediment before settlement; and (ii) the stronger current and tidal straining effect causing the significantly high resuspension after heavy rain [50].

5. Conclusions

To our knowledge, this is the first study on monitoring water quality, especially turbidity, in Cam Ranh Bay and Thuy Trieu Lagoon, using remote sensing. This study presented a method to estimate turbidity as well as the possibility of mapping water quality in a turbid deep water from remotely sensing data. A regional algorithm was developed and successfully applied to Landsat 8 OLI images to retrieve surface turbidity in the study area. The observed and computed turbidity by using Landsat 8 OLI were highly consistent, which indicates that the proposed model could be used to retrieve turbidity in high turbid waters like Cam Ranh Bay and Thuy Trieu Lagoon. Turbidity in Cam Ranh Bay and Thuy Trieu Lagoon was controlled by resuspension of bed sediment and influence of a large amount of precipitation, during both the rainy season and dry season. We demonstrated that resuspension of bed sediment is a major process controlling turbidity in shallow waters and near coastlines while rainfall is a key factor affecting turbidity in deep waters. The approach based on spatiotemporal scale is essential to determine and correctly interpret the differential effects engendered by the turbidity controlling processes in Cam Ranh Bay and Thuy Trieu Lagoon. The results can serve as a basis for future observations of turbidity pattern change in Cam Ranh Bay and Thuy Trieu Lagoon and can be applied for other similar waters. Some possible solutions proposed to decrease turbidity in the study area are minimizing the dredging works, and good control of the operation of dams and reservoirs in the upstream and aquaculture activities in the study area. To reduce the effect of wind resulting in resuspension of bed sediment, planting trees around the entire area is encouraged.

Acknowledgments: The authors would like to thank researchers working in Institute of Oceanography, Tong Phuoc Hoang Son, Le Thi Vinh, Phan Minh Thu and Bui Hong Long, for their kind supports in this research. We also thank Hae Chong O at the University of Tokyo and Sylvain Ouillon at the University of Toulouse who advised and commented on the paper. This study was partially funded by JSPS KAKENHI Grant No. 25303016.

Author Contributions: Quang Nguyen Hao and Jun Sasaki conceived the study; Quang Nguyen Hao, Jun Sasaki and Higa Hiroto organized the field trip and designed the numerical experiments; Huan Nguyen Huu provided water quality data and bathymetric and conducted experiments; Quang Nguyen Hao performed the simulations and remote sensing data processing; Quang Nguyen Hao, Jun Sasaki and Higa Hiroto analyzed the data and simulations; Quang Nguyen Hao, Higa Hiroto and Huan Nguyen Huu wrote the paper; and Jun Sasaki edited the final manuscript.

Conflicts of Interest: The authors declare no conflict of interest.

References

1. Güttler, F.N.; Niculescu, S.; Gohin, F. Turbidity retrieval and monitoring of Danube Delta waters using multisensor optical remote sensing data: An integrated view from the delta plain lakes to the western–northwestern Black Sea coastal zone. *Remote Sens. Environ.* **2013**, *132*, 86–101. [CrossRef]
2. Zheng, G.J. *Hydrodynamics and Water Quality: Modeling Rivers, Lakes, and Estuary*; John Wiley & Sons, Inc.: Hoboken, NJ, USA, 2007; pp. 130–134.
3. Minnesota Pollution Control Agency. Turbidity: Description, Impact on Water Quality, Sources, Measures—A General Overview, USA. 2008. Available online: <https://www.pca.state.mn.us/sites/default/files/wq-iw3-21.pdf> (accessed on 18 February 2016).
4. Carson, A.B.; Benjamin, M.J.; Krista, K.B.; Daniel, B.Y.; Christian, E.Z. Reconstructing turbidity in a glacially influenced lake using the Landsat TM and ETM+ surface reflectance climate data record archive, Lake Clark, Alaska. *Remote Sens.* **2015**, *7*, 13692–13710. [CrossRef]
5. Aksnes, D.L.; Dupont, N.; Staby, A.; Fiksen, Ø.; Kaartvedt, S.; Aure, J. Coastal water darkening and implications for mesopelagic regime shifts in Norwegian fjords. *Mar. Ecol. Prog. Ser.* **2009**, *387*, 39–49. [CrossRef]

6. Gernez, P.; Barille, L.; Lerouxel, A.; Mazeran, C.; Lucas, A.; Doxaran, D. Remote sensing of suspended particulate matter in turbid oyster farming ecosystems. *J. Geophys. Res. Oceans* **2014**, *119*, 7277–7294. [CrossRef]
7. Dogliotti, A.I.; Ruddick, K.G.; Nechad, B.; Doxaran, D.; Knaeps, E. A single algorithm to retrieve turbidity from remotely-sensed data in all coastal and estuarine waters. *Remote Sens. Environ.* **2015**, *156*, 157–168. [CrossRef]
8. Allan, M.G.; Hamilton, D.P.; Hicks, B.J.; Brabyn, L. Landsat remote sensing of chlorophyll a concentrations in central North Island lakes of New Zealand. *Int. J. Remote Sens.* **2011**, *32*, 2037–2055. [CrossRef]
9. Phan, M.T.; Tong, P.H.S.; Teruhisa, K. Using remote sensing technique for analyzing temporal changes of seagrass beds by human impacts in waters of Cam Ranh Bay, Vietnam. In *Remote Sensing of the Marine Environment II, 85250T, Proceedings of the SPIE8525, San Diego, CA, USA, 11 December 2012*; Frouin, R.J., Ebuchi, N., Pan, D., Saino, T., Eds.; SPIE: Kyoto, Japan, 2012.
10. Phan, M.T.; Nguyen, H.H.; Bui, H.L. Study on environmental capacity in Cam Ranh Bay and Thuy Trieu Lagoon. *J. Mar. Sci. Technol.* **2013**, *13*, 371–381. [CrossRef]
11. Vanhellemont, Q.; Ruddick, K. Turbid wakes associated with offshore wind turbines observed with Landsat 8. *J. Remote Sens. Environ.* **2014**, *145*, 105–115. [CrossRef]
12. Kishino, M.; Tanaka, A.; Joji, I. Retrieval of Chlorophyll a, suspended solids, and colored dissolved organic matter in Tokyo Bay using ASTER data. *Remote Sens. Environ.* **2005**, *99*, 66–74. [CrossRef]
13. Lim, H.S.; Matjafri, M.Z.; Abdullah, K.; Asadpour, R. A Two-Band algorithm for total suspended solid concentration mapping using THEOS data. *J. Coast. Res.* **2012**, *29*, 624–630. [CrossRef]
14. Tebbs, E.J.; Remedios, J.J.; Harper, D.M. Remote sensing of chlorophyll-a as a measure of cyanobacterial biomass in Lake Bogoria, a hypertrophic, saline-alkaline, flamingo lake, using Landsat ETM+. *Remote Sens. Environ.* **2013**, *135*, 92–106. [CrossRef]
15. Zhang, Y.; Zhang, Y.; Shi, K.; Zha, Y.; Zhou, Y.; Liu, M. A Landsat 8 OLI-Based, semianalytical model for estimating the total suspended matter concentration in the slightly turbid Xin'anjiang reservoir (China). *IEEE J. Sel. Top. Appl. Earth Obs. Remote Sens.* **2016**, *9*, 398–413. [CrossRef]
16. Doxaran, D.; Froidefond, J.M.; Castaing, P.; Babin, M. Dynamics of the turbidity maximum zone in a macrotidal estuary (the Gironde, France): Observations from field and MODIS satellite data. *Estuar. Coast. Shelf Sci.* **2009**, *81*, 321–332. [CrossRef]
17. Petus, C.; Chust, G.; Gohin, F.; Doxaran, D.; Froidefond, J.M.; Sagarminaga, Y. Estimating turbidity and total suspended matter in the Adour River plume (South Bay of Biscay) using MODIS 250-m imagery. *Cont. Shelf Res.* **2010**, *30*, 379–392. [CrossRef]
18. Ouillon, S.; Douillet, P.; Petrenko, A.; Neveux, J.; Dupouy, C.; Froidefond, J.M.; Andréfouët, S.; Caravaca, A.M. Optical algorithms at satellite wavelengths for Total Suspended Matter in tropical coastal waters. *Sensor* **2008**, *8*, 4165–4185. [CrossRef] [PubMed]
19. Ali, P.Y.; Jie, D.; Sravanthi, N. Remote sensing of chlorophyll-a as a measure of red tide in Tokyo Bay using hotspot analysis. *J. Remote Sens. Appl. Soc. Environ.* **2015**, *2*, 11–25. [CrossRef]
20. Zhang, C.; Han, M. Mapping chlorophyll-a concentration in Laizhou Bay using Landsat 8 OLI data. In Proceedings of the E-proceedings of the 36th IAHR World Congress, The Hague, the Netherlands, 28 June–3 July 2015.
21. Tong, P.H.S.; Truong, M.C.; Hoang, C.T. Detecting chlorophyll-a concentration and bloom patterns at upwelling area in South central Vietnam by high resolution multi-satellite data. *J. Environ. Sci. Eng. A* **2015**, *4*, 215–224. [CrossRef]
22. Bui, H.L.; Tran, V.C.; Nguyen, H.H.; To, D.T. Self-cleaning ability by the tide of Cam Ranh Bay—Thuy Trieu Lagoon (Khanh Hoa). *J. Sci. Technol. Environ.* **2013**, *2*, 20–22.
23. Greenberg, A.E.; Clescert, L.S.; Eaton, A.D. *Standard Methods for the Examination of Water and Wastewater*, 18th ed.; Method 2540D; American Public Health Association: Washington, DC, USA, 1992; pp. 2–56.
24. Parsons, T.R.; Maita, Y.; Lalli, M.C. *A Manual of Chemical and Biological Methods for Seawater Analysis*; Pergamon Press: Oxford, UK, 1984; pp. 110–173.
25. Adam, T. Remote Sensing Models of Algal Blooms and Cyanobacteria in Lake Champlain. Master's Thesis, Department of Civil and Environmental Engineering of the University of Massachusetts Amherst, Amherst, MA, USA, February 2012.
26. Retsch GmbH Haan. Sieve Analysis Taking a Close Look at Quality. 2009. Available online: http://www.mep.net.au/wpcontent/uploads/2013/07/MEP_expert_guide_sieving_en.pdf (accessed on 15 March 2016).

27. Wesley, J.M.; Anatoly, A.G.; Richard, L.P.; Daniela, G.; Donald, C.R.; Bryan, C.L.; Tadd, M.B.; Paul, B. Estimation of chlorophyll-a concentration in turbid productive waters using airborne hyperspectral data. *Water Res.* **2012**, *46*, 993–1004. [[CrossRef](#)]
28. Kaliraj, S.; Chandrasekar, N.; Mages, N.S. Multispectral image analysis of suspended sediment concentration along the Southern coast of Kanyakumari, Tamil Nadu, India. *J. Coast. Sci.* **2014**, *1*, 63–71.
29. Jorge, D.S.F.; Amore, D.J.; Barbossa, C.F. Efficiency estimation of four different atmospheric correction algorithms in a sediment-loaded tropic lake for Landsat 8 OLI sensor. In Proceedings of the Anais XVII Simpósio Brasileiro de Sensoriamento Remoto—SBSR, João Pessoa-PB, Brasil, 25–29 April 2015.
30. Watanabe, F.; Sayuri, Y.; Enner, A.; Thanan, W.; Pequeno, R.; Nilton, N.I.; Cláudio, C.F.B.; Luiz, H.S.R. Estimation of chlorophyll-a concentration and the trophic state of the Barra Bonita Hydroelectric Reservoir using OLI/Landsat 8 images. *Int. J. Environ. Res. Public Health* **2015**, *12*, 10391–10417. [[CrossRef](#)] [[PubMed](#)]
31. ENVI. *Atmospheric Correction Module: QUAC and FLAASH User's Guide*; EXELIS Visual Information Solutions: Boulder, CO, USA, 2009.
32. Ouillon, S.; Douillet, P.; Andrefouet, S. Coupling satellite data with in situ measurements and numerical modeling to study fine suspended-sediment transport: A study for the lagoon of New Caledonia. *Coral Reefs* **2004**, *23*, 109–122. [[CrossRef](#)]
33. Hellweger, F.L.; Schlossera, P.; Lalla, U.; Weissel, J.K. Use of satellite imagery for water quality studies in New York Harbor. *Estuar. Coast. Shelf Sci.* **2004**, *61*, 437–448. [[CrossRef](#)]
34. Lim, J.; Choi, M. Assessment of water quality based on Landsat 8 operational land imager associated with human activities in Korea. *J. Environ. Monit. Assess.* **2015**, *187*, 384. [[CrossRef](#)] [[PubMed](#)]
35. Ritchie, C.J.; Zimba, V.P.; Everitt, H.J. Remote sensing techniques to assess water quality. *Photogramm. Eng. Remote Sens.* **2003**, *69*, 695–704. [[CrossRef](#)]
36. Booij, N.; Ris, R.C.; Holthuijsen, L.H. A third-generation wave model for coastal regions. *J. Geophys. Res.* **1999**, *104*, 7667–7681. [[CrossRef](#)]
37. SWAN Team. Swan Scientific and Technical Documentation: SWAN Cycle III Version 41.01AB. Delft University of Technology, The Netherlands, 2015. Available online: <http://swanmodel.sourceforge.net/download/zip/swantech.pdf> (accessed on 20 February 2016).
38. Dalyander, P.S.; Butman, B.; Sherwood, R.C.; Signell, P.R.; Wilkin, L.J. Characterizing wave- and current-induced bottom shear stress: U.S. middle Atlantic continental shelf. *Cont. Shelf Res.* **2013**, *52*, 73–86. [[CrossRef](#)]
39. Phan, T.B. Process Simulation the Transmission of Pollutants under Impacts of Dynamic Factors in Cam Ranh Bay by Using Numerical Models. Master Thesis of Department of Meteorology, Hydrology and Oceanography, Ha Noi University of Science, Ha Noi, Vietnam, 2012. Available online: [http://hus.vnu.edu.vn/files/ChuaPhanLoai/LuanVanThacSi-ChuaPhanLoai%20\(423\).pdf](http://hus.vnu.edu.vn/files/ChuaPhanLoai/LuanVanThacSi-ChuaPhanLoai%20(423).pdf) (accessed on 10 April 2016).
40. Rasmemasuang, T.; Sasaki, J. Modeling of mud accumulation and bed characteristics in Tokyo Bay. *Coast. Eng. J.* **2008**, *50*, 277–308. [[CrossRef](#)]
41. Sheng, P.Y.; Lick, W. The Transport and Resuspension of Sediments in a Shallow Lake. *J. Geophys. Res.* **1979**, *84*, 1809–1826. [[CrossRef](#)]
42. Bonansea, M.; Rodriguez, M.C.; Pinotti, L.; Ferrero, S. Using multi-temporal Landsat imagery and linear mixed models for assessing water quality parameters in Río Tercero reservoir (Argentina). *Remote Sens. Environ.* **2015**, *158*, 28–41. [[CrossRef](#)]
43. Lobo, F.L.; Costa, M.P.F.; Novo, E.M.L.M. Time-series analysis of Landsat-MSS/TM/OLI images over Amazonian waters impacted by gold mining activities. *Remote Sens. Environ.* **2013**, *157*, 170–184. [[CrossRef](#)]
44. Garaba, S.P.; Zielinski, O. An assessment of water quality monitoring tools in an estuarine system. *J. Remote Sens. Appl. Soc. Environ.* **2015**, *2*, 1–10. [[CrossRef](#)]
45. Fang, S.; Suhyb, S.M.H.D.; Zhou, Y.X.; Li, J.F.; Su, Z.; Kuang, D.B. Remote-sensing reflectance characteristics of highly turbid estuarine waters—A comparative experiment of the Yangtze River and the Yellow River. *Int. J. Remote Sens.* **2010**, *31*, 2639–2654.
46. Vanhellemont, Q.; Ruddick, K. Advantages of high quality SWIR bands for ocean colour processing: Examples from Landsat 8. *Remote Sens. Environ.* **2015**, *161*, 89–106. [[CrossRef](#)]
47. Zhubin, Z.; Yunmei, L.; Yulong, G.; Yifan, X.; Ge, L.; Chenggong, D. Landsat-based long-term monitoring of total suspended matter concentration pattern change in the wet season for Dongting Lake, China. *Remote Sens.* **2015**, *7*, 13975–13999. [[CrossRef](#)]

48. Richardson, J.; Jowett, I.G. Effects of sediment on fish communities in East Cape streams, North Island, New Zealand. *N. Z. J. Mar. Freshw. Res.* **2002**, *36*, 431–442. [[CrossRef](#)]
49. Goransson, G.; Larson, M.; Bendz, D. Variation in turbidity with precipitation and flow in a regulated river system—River GötaÄlv, SW Sweden. *Hydrol. Earth Syst. Sci.* **2013**, *17*, 2529–2542. [[CrossRef](#)]
50. Yu, Y.; Zhang, H.; Lemckert, C. Salinity and turbidity distributions in the Brisbane River estuary, Australia. *J. Hydrol.* **2014**, *519*, 3338–3352. [[CrossRef](#)]



© 2017 by the authors. Licensee MDPI, Basel, Switzerland. This article is an open access article distributed under the terms and conditions of the Creative Commons Attribution (CC BY) license (<http://creativecommons.org/licenses/by/4.0/>).